Low PAPR FBMC

Dongjun Na and Kwonhue Choi, *Senior Member, IEEE*

***Abstract*— Unlike single carrier-frequency division multiple access (SC-FDMA), just combining discrete Fourier transform (DFT) spreading and filter bank multicarrier with offset quadrature amplitude modulation (FBMC-OQAM) results in only marginal peak to average power ratio (PAPR) reduction. To utilize the single carrier effect of DFT spreading, a special condition of the coefficients at each subcarrier's in-phase and quadrature-phase (IQ) channels should be satisfied. As a starting point, we first derive this condition, which we call the identically-time-shifted-multicarrier (ITSM) condition. Then, based on this condition, we propose a new type of FBMC for low PAPR. The main features of the proposed scheme are summarized as follows. First, in order to further enhance the amount of PAPR reduction, we generate the four candidate versions of the DFT-spread and ITSM-conditioned FBMC waveform and select the one with minimum peak power. Even with multiple candidate generation, the major computation parts, such as DFT and IDFT are shared and need to be performed only once, unlike the conventional side information (SI)-based PAPR reduction schemes. Consequently, with a fractional complexity overhead compared with the previous DFT-spread FBMC, the proposed scheme achieves a PAPR reduction comparable to that of SC-FDMA. Second, the proposed scheme transmits only two bit SI per data block consisting of multiple FBMC-OQAM symbols. Hence, the SI overhead is significantly low compared with the usual SI-based schemes, such as selective mapping or partial transmit sequence.**

***Index Terms*— FBMC (filter bank multicarrier), PAPR (peak-to-average power ratio), OQAM (offset QAM), HPA (high power amplifier), SC-FDMA (single carrier FDMA).**

I. Introduction

AT PRESENT, the FBMC-OQAM (filter bank multicarrier with offset quadrature amplitude modulation) gains considerable attention for future wireless systems. Although FBMC[1] has a significant number of merits, there are still some issues that need to be resolved. For instance, as the FBMC is based on multicarrier modulation, it has a high PAPR (peak to average power ratio). A high PAPR could cause signal clipping or other nonlinearities to the FBMC signal. Even with a slight nonlinearity, there will be a considerable boost in the OOB (out of band) spectrum and the intrinsic advantage of FBMC, i.e., superb OOB spectrum suppression vanishes [1]–[3].

Due to the IQ (In-phase and Quadrature-phase)-staggered and pulse-shaped structure of OQAM, the existing methods for lowering the PAPR of OFDM (orthogonal frequency division multiplexing) need to be modified before applying them to FBMC. Two typical SI (side information)-based PAPR reduction schemes for OFDM, i.e., PTS (partial transmit sequence) and SLM (selective mapping) have been modified for the application to FBMC in [4], [5], and [6]–[9], respectively. These schemes mainly search the best candidates jointly over the multiple FBMC symbols to take care of the signal structure of FBMC in which the consecutive symbols are overlapped due to pulse shaping and IQ staggering of OQAM. Basically, all these SI-based PAPR reduction schemes have the drawback of SI burden, which leads to reduced data efficiency. Another drawback is that compared to the basic FBMC, these schemes require the considerable computation complexity overhead for the candidate signal generation and selection. Moreover, for taking into account the overlapped signal structure of the pulse shaped OQAM, even higher complexities are required compared to the SI-based PAPR reduction schemes for OFDM. The segment-based PTS scheme in [5] requires less, but still high, complexity, and the data rate is sacrificed by non-negligible periodic zero insertions between the consecutive small segments. In [10], the SWTR (sliding window tone reservation) method for FBMC shows favorable PAPR reduction gain. However, it requires a considerable number of iterations, and results in significant loss of energy and bandwidth for the reserved tones, for instance, 12.5 % loss according to the setting used in [10].

In this paper, we aim to propose a new type of FBMC, whose waveform has an inherently low PAPR without the use of any of the complicated PAPR reduction schemes mentioned above. The two main design factors that we consider are *low complexity overhead* and *negligible SI overhead*. In the context of OFDM, we have a good solution example, which is called SC-FDMA (single carrier-frequency division multiple access). In SC-FDMA, nothing but DFT spreading is performed prior to the OFDM modulation. The DFT spreading technique has two distinguishable merits compared to the other PAPR schemes. Firstly, the complexity overhead is minimal, as only DFT and IDFT are additionally needed at the transmitter and receiver sides, respectively. Secondly, the receiver does not require SI because both the DFT operation and its inversion operation are deterministic. Hence, extending the DFT spreading-based approach to FBMC well matches our design goal. In [11]–[13], just like SC-FDMA, the DFT-spread FBMC, in which DFT is performed prior to

Manuscript received December 10, 2016; revised May 30, 2017 and August 12, 2017; accepted October 10, 2017. Date of publication October 20, 2017; date of current version January 8, 2018. This work was supported in part by Basic Science Research Program through the National Research Foundation funded by the Ministry of Education, South Korea, under Grant 2015R1D1A3A01015970, and in part by the Ministry of Science and ICT, South Korea, under the Information Technology Research Center Support Program supervised by the Institute for Information and Communications Technology Promotion under Grant IITP-2017-2016-0-00313. The associate editor coordinating the review of this paper and approving it for publication was T. Zemen. *(Corresponding author: Kwonhue Choi.)*

The authors are with the Department of Information and Communication Engineering, Yeungnam University, Gyeongsan 38541, South Korea (e-mail: nadj2964@ynu.ac.kr; gonew@yu.ac.k).

Color versions of one or more of the figures in this paper are available online at http://ieeexplore.ieee.org.

Digital Object Identifier 10.1109/TWC.2017.2764028

[1]Hereafter, FBMC refers to FBMC-OQAM for simplicity.

the FBMC modulator, was investigated. However, the PAPR reduction with this technique is not as impressive as that with SC-FDMA. Therefore, in [11] and [12], they have also proposed an FB (filter bank)-spread FBMC and showed that the FB-spread FBMC provides a much lower PAPR than that provided by the DFT-spread FBMC. However, the FB-spread FBMC requires a higher computation complexity compared to the DFT-spread FBMC. Moreover, due to the spreading transform, it is less bandwidth-efficient than the DFT-spread FBMC.

In order to inherit the merits of DFT-spreading from OFDM to FBMC as it matches our design goal, i.e., low complexity and negligible SI overhead, we need to resolve the issues of the previous DFT-spread FBMC schemes. This motivated us to analyze the FBMC signal format in comparison with the OFDM signal format in this perspective. We found that the small PAPR reduction in the previous DFT-spread FBMCs in [11]–[13] is due to the fact that the employed FBMC modulator structures do not accommodate the single carrier effect of DFT spreading. To maximally utilize the single carrier effect of DFT spreading, a special condition of the phase shift terms for each subcarrier's IQ channels should be satisfied, in addition to the basic requirement for the FBMC waveform format. Our work starts from deriving this special condition for FBMC, which we call *ITSM (identically time shifted multicarrier)* condition.

In this paper, basically based on the combination of DFT spreading and ITSM-conditioned FBMC, we propose a new type of FBMC for low PAPR. With a fractional complexity overhead compared to that of the previous DFT-spread FBMC, the proposed scheme achieves a PAPR reduction comparable to that of SC-FDMA. The usual SI-based PAPR reduction schemes, such as SLM or PTS, require considerable number of computations, which is up to several times that of the proposed scheme. Apart from the substantial PAPR reduction, the SI overhead of the proposed scheme is significantly low compared to the usual SI-based PAPR reduction schemes.

The remainder of this paper is structured as follows: In Section II, we survey the implementation structures of the FBMC and the previous DFT-spread FBMC. In Section III, we show that for the DFT-spread FBMC, the commonly used phase shift patterns for FBMC are not optimal in terms of PAPR performance and then, we derive the special condition of the phase shift pattern, which substantially improves PAPR performance. In Section IV, based on the result in Section III and combining it with a candidate selection scheme requiring negligible SI, we propose a new type of FBMC for low PAPR and provide its implementation structure. The equivalent conversions to the complexity reduced structure are explained in detail. In Section V, the PAPR performance and the computation complexity are assessed in comparison with the existing PAPR reduction schemes for FBMC. Finally in Section VI, the concluding remarks are provided.

II. Review of FBMC and DFT-Spread FBMC

Throughout this paper, we use the following notations: $\Re\{x\}$ = real part of x, $\Im\{x\}$ = imaginary part of x and $[x_n]_{n=a}^{b} \triangleq [x_a, x_{a+1}, \cdots, x_b]$. Fig. 1(a) shows the state

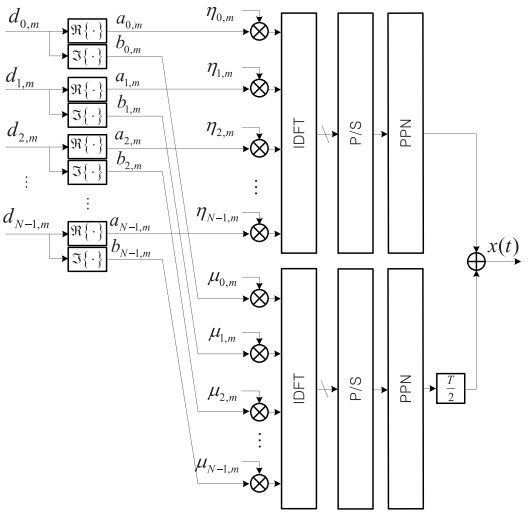

(a) Implementation structure of FBMC

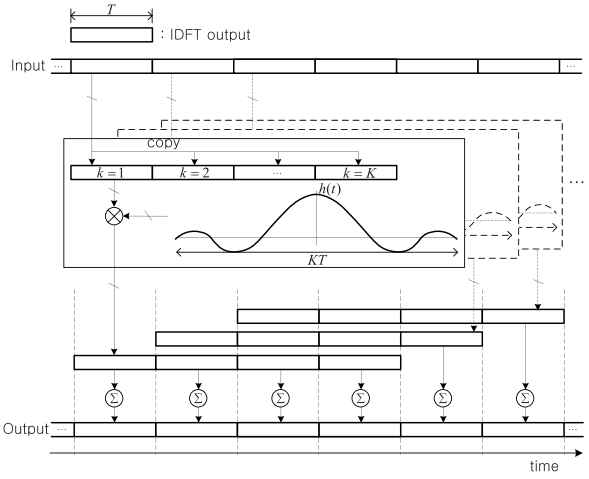

(b) An explicit implementation of PPN

Fig. 1. Implementation structure of FBMC and PPN.

of art implementation structure of the FBMC modulator [14], [15]. The number of subcarriers is denoted by N. The mth complex input symbol on the nth carrier is denoted by $d_{n,m}$. If we express $d_{n,m}$ as

$$d_{n,m} = a_{n,m} + jb_{n,m} \tag{1}$$

where $a_{n,m}$ and $b_{n,m}$ denote the real and imaginary data terms, respectively, then $a_{n,m}$ and $b_{n,m}$ are split and fed into upper and lower IDFTs with the phase shift terms multiplied. The phase shift term of $a_{n,m}$ (at the nth element of upper IDFT input vector) is denoted by $\eta_{n,m}$ and the phase shift term of $b_{n,m}$ (at the nth element of lower IDFT input vector) is denoted by $\mu_{n,m}$, as shown in Fig. 1(a). In order to comply with the FBMC signal format, $\eta_{n,m}$ and $\mu_{n,m}$ must satisfy the following rule [14], [16]:

$$\eta_{n,m} = \begin{cases} 1(\text{or} -1) & \text{if } n = \text{even}, \\ j(\text{or} -j) & \text{if } n = \text{odd}, \end{cases}$$
$$\mu_{n,m} = \begin{cases} j(\text{or} -j) & \text{if } n = \text{even}, \\ 1(\text{or} -1) & \text{if } n = \text{odd}. \end{cases} \tag{2}$$

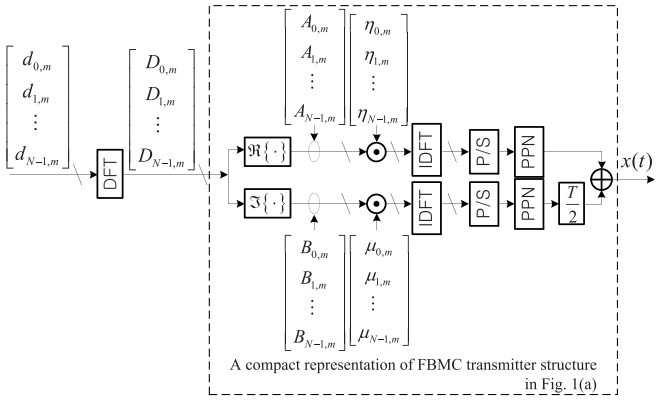

Fig. 2. Implementation structure of DFT-spread FBMC, $\odot$ denotes element-by-element multiplication.

Using the PPN (polyphase network) technique [14], the individual pulse-shaping of each subcarrier can be performed at once at the output stage of IDFT, as shown in Fig. 1(a). With the overlap-and-sum technique [14], [15], [17], the PPN can be explicitly implemented as shown in Fig. 1(b) where T denotes the complex data symbol duration of each subcarrier, $h(t)$ denotes the impulse response of the pulse shaping prototype filter, and K denotes the overlapping factor of the pulse. The operation of the PPN in Fig. 1(b) is explained as follows [15]: First, each IDFT output vector is copied K times and is repeated. Then, the sampled version of $h(t)$ over K symbol duration is multiplied to the repeated IDFT output vector. This is successively performed for every IDFT output vector as illustrated in stacked boxes of Fig. 1(b). Finally, as shown in the lower part of Fig. 1(b), each of the multiplied vectors is aligned with its corresponding input (= IDFT output) vector timing and then, is added together to generate the output sequence of the PPN. To introduce 1/2 symbol timing offset between IQ channels for OQAM, the output of the lower PPN in Fig. 1(a) passes through $T/2$-delay block.

In [11]–[13], inspired by the SC-FDMA, the authors investigated the DFT-spread FBMC as shown in Fig. 2. In the DFT-spread FBMC in [11]–[13], the DFT-spread data vector is directly fed to the FBMC input. Let the complex vector $\left[D_{n,m}\right]_{n=0}^{N-1}$ $\left(=\left[A_{n,m}+jB_{n,m}\right]_{n=0}^{N-1}\right)$ denote the DFT output vector when the DFT input vector is the data symbol vector $\left[d_{n,m}\right]_{n=0}^{N-1}$ $\left(=\left[a_{n,m}+jb_{n,m}\right]_{n=0}^{N-1}\right)$ as shown in Fig. 2.

III. Phase Shift Pattern Condition for the Single Carrier Effect of the DFT-Spread FBMC

A. Problems With the Commonly Used Phase Shift Patterns

One of the most commonly used phase shift patterns satisfying the rule in (2) is given as follows [5], [18]–[23]:

$$\eta_{n,m} = j^{n+2m} \quad \text{or } (-1)^m j^n \tag{3}$$

$$\mu_{n,m} = j^{n+2m+1} \quad \text{or } (-1)^m j^{n+1}. \tag{4}$$

This pattern is expressed in different ways in the literature due to the use of different notations; however, they are all equivalent. For instance, (3) and (4) are often equivalently expressed as $\eta_{n,m} = e^{j\phi_{n,2m}}$ and $\mu_{n,m} = e^{j\phi_{n,2m+1}}$, where $\phi_{n,k} = \pi(n+k)/2$ [18]–[20]. It should be noted that m is the complex symbol index whereas k of $\phi_{n,k} = \pi(n+k)/2$ is the real symbol index and therefore, $\eta_{n,m}$ and $\mu_{n,m}$ correspond to the phase shift terms of the $2m$-th and the $(2m+1)$-th real symbols, respectively.

Let us check whether or not the DFT-spread FBMC achieves the single carrier effect like SC-FDMA, for the case when the phase shift pattern in (3) and (4) is used. As IDFT followed by PPN, which is shown in Fig. 2, is equivalent to per-carrier pulse shaping followed by multicarrier modulation [14], the continuous version of the transmit waveform $x(t)$ is written as follows:

$$\begin{aligned} x(t) &= \sum_{n=0}^{N-1}\left\{\sum_{m=0}^{M-1}(-1)^m j^n A_{n,m}h(t-mT)\right\}e^{jn\frac{2\pi}{T}t} \\ &\quad + \sum_{n=0}^{N-1}\left\{\sum_{m=0}^{M-1}(-1)^m j^{n+1} B_{n,m}h\left(t-mT-\frac{T}{2}\right)\right\}e^{jn\frac{2\pi}{T}\left(t-\frac{T}{2}\right)} \\ &= \sum_{n=0}^{N-1}\sum_{m=0}^{M-1}(-1)^m\left\{A_{n,m}h(t-mT)e^{jn\frac{2\pi}{T}\left(t+\frac{T}{4}\right)}\right. \\ &\quad \left. + jB_{n,m}h\left(t-mT-\frac{T}{2}\right)e^{jn\frac{2\pi}{T}\left(t+\frac{T}{4}-\frac{T}{2}\right)}\right\} \end{aligned} \tag{5}$$

where M denotes the number of OQAM symbols per carrier in a frame. Only for ease of checking the single carrier effect, let us temporarily detach the pulse shaping effect, i.e., assume the rectangular pulse $h(t) = 1$ for $0 \le t \le T$ and 0 elsewhere. Then, for the overlapped interval of the IQ terms of the mth OQAM: $mT + T/2 \le t \le (m+1)T$, (5) is written as:

$$\begin{aligned} x(t) = (-1)^m &\left\{\sum_{n=0}^{N-1} A_{n,m}e^{jn\frac{2\pi}{T}\left(t+\frac{T}{4}\right)}\right. \\ &\left. + j\sum_{n=0}^{N-1} B_{n,m}e^{jn\frac{2\pi}{T}\left(t+\frac{T}{4}-\frac{T}{2}\right)}\right\}. \end{aligned} \tag{6}$$

Let $D_{n,m}$ denote the nth element of the DFT spread symbol vector, i.e.,

$$D_{n,m} = \sum_{k=0}^{N-1} d_{k,m}e^{-j\frac{2\pi}{N}nk}. \tag{7}$$

Then, from Fig. 2, we have $A_{n,m} = \Re\{D_{n,m}\} = \frac{D_{n,m}+D_{n,m}^*}{2}$, and $B_{n,m} = \Im\{D_{n,m}\} = \frac{D_{n,m}-D_{n,m}^*}{2j}$. Thus, (6) is written as

$$\begin{aligned} x(t) = \frac{(-1)^m}{2}&\left(\sum_{n=0}^{N-1} D_{n,m}e^{jn\frac{2\pi}{T}\left(t+\frac{T}{4}\right)} + \sum_{n=0}^{N-1} D_{n,m}^* e^{jn\frac{2\pi}{T}\left(t+\frac{T}{4}\right)}\right. \\ &\left. + \sum_{n=0}^{N-1} D_{n,m}e^{jn\frac{2\pi}{T}\left(t+\frac{T}{4}-\frac{T}{2}\right)} - \sum_{n=0}^{N-1} D_{n,m}^* e^{jn\frac{2\pi}{T}\left(t+\frac{T}{4}-\frac{T}{2}\right)}\right) \end{aligned} \tag{8}$$

Substituting (7) into (8), the first summation term is derived as follows:

$$\begin{aligned}\sum_{n=0}^{N-1} D_{n,m} e^{jn\frac{2\pi}{T}\left(t+\frac{T}{4}\right)} &= \sum_{n=0}^{N-1}\left(\sum_{k=0}^{N-1} d_{k,m} e^{-j\frac{2\pi}{N}nk}\right) e^{jn\frac{2\pi}{T}\left(t+\frac{T}{4}\right)} \\ &= \sum_{k=0}^{N-1} d_{k,m} \sum_{n=0}^{N-1} e^{j\frac{2\pi n}{T}\left(t-\frac{T}{N}k+\frac{T}{4}\right)} \\ &= \sum_{k=0}^{N-1} d_{k,m} f\left(t-\frac{T}{N}k+\frac{T}{4}\right) \end{aligned} \quad (9)$$

where

$$f(t) = \sum_{n=0}^{N-1} e^{j\frac{2\pi n}{T}t} = \frac{\sin\left(\frac{\pi N}{T}t\right)}{\sin\left(\frac{\pi}{T}t\right)} e^{j\frac{(N-1)\pi}{T}t}. \quad (10)$$

The pulse magnitude $|f(t)|$ is determined by the term $\frac{\sin\left(\frac{\pi N}{T}t\right)}{\sin\left(\frac{\pi}{T}t\right)}$, which is equal to the Dirichlet sinc pulse [24]. As N increases, the pulse width gets narrower. Note that the symbol index k (the FBMC subcarrier index) affects not the frequency but the shift of the pulse $f\left(t-\frac{T}{N}k+\frac{T}{4}\right)$ in (9). Overall, $f\left(t-\frac{T}{N}k+\frac{T}{4}\right)$ is the shifted version of the baseband narrow pulse. Consequently, (9) is equal to a single carrier signal, which sequentially transmits the T/N-spaced and data symbol-multiplied narrow pulses.

There is a timing offset $\frac{T}{4}$ in the data symbol-multiplied pulse train in the summation of (9). By using the fact that $f(t)$ is a periodic function with a period of T, we change the expression of (9) as follows:

$$\sum_{k=0}^{N-1} d_{k,m} f\left(t-\frac{T}{N}k+\frac{T}{4}\right) = \sum_{k=0}^{N-1} d_{\left[\left(k+\frac{N}{4}\right)\bmod N\right],m} f\left(t-\frac{T}{N}k\right) \quad (11)$$

where the operation $[a \bmod b]$ denotes a modulo b. In the changed expression, the timing offset of the data symbol-multiplied pulse train is 0 not $T/4$, but the data symbol sequence is cyclic shifted, instead. Similarly, after some tedious manipulations, the other three summation terms in (8) are derived as the single carrier signals like the right hand side expression of (11) but with different data symbol (or its conjugate) indices at the same pulse positions. Substituting these single carrier forms for the four summations into (8), $x(t)$ is refined as follows:

$$\begin{aligned} x(t) = \frac{(-1)^m}{2} \sum_{k=0}^{N-1} \Bigg(& d_{\left[\left(k+\frac{N}{4}\right)\bmod N\right],m} + d^*_{\left[\left(\frac{3N}{4}-k\right)\bmod N\right],m} \\ & + d_{\left[\left(k-\frac{N}{4}\right)\bmod N\right],m} - d^*_{\left[\left(\frac{5N}{4}-k\right)\bmod N\right],m} \Bigg) f\left(t-\frac{T}{N}k\right). \end{aligned} \quad (12)$$

Note that despite the single carrier expression, four different symbols are added at the same symbol timings. We can expect some PAPR reduction compared to pure (Non-DFT-spread) FBMC because in the pure FBMC, $N(\gg 4)$ different symbols are added at the same symbol timing in parallel by the multicarrier modulation. However, compared to the SC-FDMA or other normal single carrier signals, the PAPR is substantially high due to the four different symbols added at the symbol timings. After all, the phase shift pattern in (3) and (4) fails to fully exploit the single carrier effect of DFT-spreading.

B. Phase Shift Condition for Single Carrier Effect: ITSM Condition

We can rewrite (6) as follows:

$$x(t) = (-1)^m \sum_{n=0}^{N-1} \left\{A_{n,m} + j(-1)^n B_{n,m}\right\} e^{jn\frac{2\pi}{T}\left(t+\frac{T}{4}\right)}. \quad (13)$$

Suppose the term $(-1)^n$ ahead of $B_{n,m}$ does not exist, then (13) is written as:

$$x(t) = (-1)^m \sum_{n=0}^{N-1} D_{n,m} e^{jn\frac{2\pi}{T}\left(t+\frac{T}{4}\right)}. \quad (14)$$

Note that the summation in (14) is equal to (9). This implies that without the term $(-1)^n$ ahead of $B_{n,m}$ in (13), $x(t)$ is a pure single carrier signal.

In order to cancel the term $(-1)^n$, we need to pre-compensate $B_{n,m}$ in (13) by multiplying $(-1)^n$ to $B_{n,m}$, since we get $(-1)^n\left\{(-1)^n B_{n,m}\right\} = B_{n,m}$. In terms of the input to the IDFT in the lower part (delayed branch) of Fig. 2, this pre-compensation is equivalent to multiplying $(-1)^n$ to $\mu_{n,m}$ instead of $B_{n,m}$, and thus it is equivalent to setting $\mu_{n,m}$ as follows:

$$\begin{aligned}\mu_{n,m} &= (-1)^n \times \left(\mu_{n,m} \text{ in (4)}\right) = (-1)^n (-1)^m j^{n+1} \\ &= (-1)^m j (-j)^n \end{aligned} \quad (15)$$

which also satisfies the basic rule of the phase shift pattern for the FBMC given in (2). The phase shift setting in (3) and (15) can be equivalently expressed as: $\eta_{n,m} = e^{j\phi_{n,2m}}$ and $\mu_{n,m} = e^{j\phi_{n,2m+1}}$ where $\phi_{n,k} = \frac{(n+k)\pi}{2} - nk\pi$.

From (6) and (13), we can figure out that the term $(-1)^n$ in (13) comes from a feature of IDFT/PPN-based FBMC structure that the $T/2$ delay block is placed necessarily *after* IDFT. Therefore, in order to fully exploit the single carrier effect, we should carefully set the phase shift terms in such a way that they cancel out the term $(-1)^n$, and thus in the final signal expression, the multicarriers for the IQ terms appear identically time shifted as in (14). We call this case 'ITSM (identically time shifted multicarriers)-conditioned' in this paper. The setting, in (3) and (15), is one of the ITSM-conditioned cases and the corresponding exact DFT-spread FBMC signal including the pulse shaping is written as follows:

$$\begin{aligned} x(t) = \sum_{n=0}^{N-1}\sum_{m=0}^{M-1} (-1)^m \Bigg\{ & A_{n,m} h(t-mT) \\ & + jB_{n,m} h\left(t-mT-\frac{T}{2}\right)\Bigg\} e^{jn\frac{2\pi}{T}\left(t+\frac{T}{4}\right)}. \end{aligned} \quad (16)$$

The time shift term $\frac{T}{4}$ at each subcarrier causes $\eta_{n,m}$ and $\mu_{n,m}$ to alternate between 1(or -1) and j(or -j) in the subcarrier axis. It is straightforward that even if we change $\frac{T}{4}$ in (16) into $-\frac{T}{4}$, the alternation still works. Hence, we can make another version

TABLE I
PHASE SHIFT PATTERNS IN THE LITERATURE ON FBMC

Pattern number	$(\eta_{n,m}, \mu_{n,m})$	Crossed C2R	ITSM-conditioned	Reference
1	((3), (15)) or ((18), (19))	×	○	this paper
2	((3), (15))	○	×	Eqns.(1-2) in [11], Eqn.(1) in [12] Eqns.(10-13) in [25]
3	((3), (4))	×	×	Eqn. (1) in [5], Eqn. (35) in [18], Fig.2 in [19], Below Eqn.(3) in [20], Eqns.(1-2) in [21], Below Eqn.(6) in [22], Eqn. (7) in [23]
4	((3), (4))	○	×	Eqn. (1) in [8]
5	$\eta_{n,m} = \begin{cases} 1 \text{ if } n = \text{even} \\ j \text{ if } n = \text{odd} \end{cases}$, $\mu_{n,m} = \begin{cases} j \text{ if } n = \text{even} \\ 1 \text{ if } n = \text{odd} \end{cases}$	×	×	Eqns.(1-2) in [26], Eqns.(1-3) in [27]
6	$\eta_{n,m} = \begin{cases} 1 \text{ if } n = \text{even} \\ j \text{ if } n = \text{odd} \end{cases}$, $\mu_{n,m} = \begin{cases} j \text{ if } n = \text{even} \\ 1 \text{ if } n = \text{odd} \end{cases}$	○	×	Eqns.(6-7) in [25], Code lines 39-45 and 76-82 in [15]
7	$\eta_{n,m} = j^n$, $\mu_{n,m} = j^{n+1}$	×	×	Fig.3 in [17], Fig.1 in [28]

of the ITSM-conditioned and DFT-spread FBMC signal as follows:

$$x(t) = \sum_{n=0}^{N-1} \sum_{m=0}^{M-1} (-1)^m \left\{ A_{n,m} h(t - mT) + j B_{n,m} h\left(t - mT - \frac{T}{2}\right) \right\} e^{jn\frac{2\pi}{T}(t-\frac{T}{4})}. \quad (17)$$

Just like we have obtained (15) from (14), we can obtain the values of $\eta_{n,m}$ and $\mu_{n,m}$ for $x(t)$ in (17) as follows:

$$\eta_{n,m} = (-1)^m (-j)^n \quad (18)$$

$$\mu_{n,m} = (-1)^m (j)^{n+1} \quad (19)$$

which also satisfy (2).

C. PAPR Comparison Among the Various FBMCs According to the Phase Shift Pattern With/Without DFT Spreading

The phase shift setting in (3) and (4) is just one of the examples that fail to achieve the single carrier effect of DFT spreading. Table I lists up the different phase settings found in the literature on FBMC. We meticulously examined the differences among FBMC signal models in the literature, such as whether $T/2$-delay is introduced before or after the multicarrier modulation stage. Then, we equivalently converted each of them into the structure shown in Fig. 1(a) to find the corresponding $\eta_{n,m}$ and $\mu_{n,m}$. In some papers, the cross mapping of C2R (complex to real) was employed for every other subcarrier, i.e., at the input stage of Fig. 1(a), they set

$$a_{n,m} = \begin{cases} \Re\{d_{n,m}\} & \text{if } n = \text{even} \\ \Im\{d_{n,m}\} & \text{if } n = \text{odd}, \end{cases}$$

$$b_{n,m} = \begin{cases} \Im\{d_{n,m}\} & \text{if } n = \text{even} \\ \Re\{d_{n,m}\} & \text{if } n = \text{odd}, \end{cases} \quad (20)$$

instead of setting $a_{n,m} = \Re\{d_{n,m}\}$ and $b_{n,m} = \Im\{d_{n,m}\}$ for all n as shown in Fig. 1(a). The column termed *'Crossed C2R'* in Table I specifies whether or not the corresponding reference employs the crossed mapping explained above. The crossed C2R does not break the FBMC signal format because it simply switches the two real valued symbols. However, with DFT spreading followed by the crossed C2R, the phase shift setting should be correspondingly changed to satisfy the ITSM condition. Through rigorous analysis as done in Section III-A, we checked whether each phase shift setting listed in Table I satisfies the ITSM condition (=condition resulting in only one single carrier form) and specified it in the column termed *'ITSM-conditioned'*.

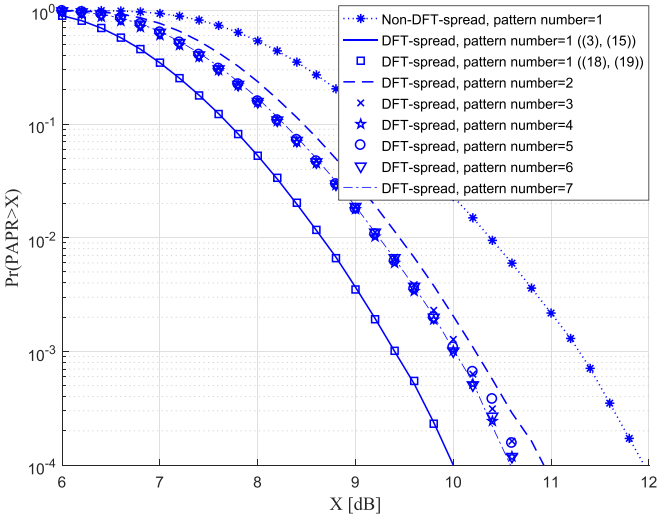

Fig. 3. CCDF of PAPR for various FBMCs according to the phase shift pattern with/without DFT spreading, $N = 160$, OQPSK and PHYDYAS prototype filter [14] with $K = 4$.

In Fig. 3, the simulated CCDFs (Complementary Cumulative Distribution Functions) of PAPR, i.e., Pr[PAPR $> X$] of the various DFT-spread FBMC waveforms using the phase shift patterns in Table I are plotted as the functions of the threshold X in dB scale. The PAPR is calculated for each FBMC symbol as follows:

$$\text{PAPR} = \frac{\max_{(m-1)T<t<mT} |x(t)|^2}{P_a}, \quad m = 0, 1, \cdots, M-1, \quad (21)$$

where P_a denotes the average power of the FBMC modulated waveform $x(t)$. For reference, the PAPRs of the pure (non-DFT-spread) FBMC waveforms are also simulated. The results reveal that the pure FBMC waveforms achieve identical PAPR performance irrespective of the phase shift pattern. Hence, the result only for case of the pattern number 1 is plotted for neat presentation. The identical PAPR performance can be intuitively explained as follows. As every phase shift

pattern should satisfy the rule in (2), the different phase shift patterns only differ in the signs of their elements. Thus, changing the phase shift pattern in Fig. 1(a) can be equivalently done by accordingly changing the signs of the IDFT input elements while fixing the phase shift pattern. The sign changes of the IDFT input elements have no influence on PAPR. This is because the data symbols $a_{n,m}$ and $b_{n,m}$ in Fig. 1(a) are already statistically independent and thus, the IDFT input elements are statistically independent, too, irrespective of changing the signs of the elements.

On the other hand, it is remarkable that the DFT-spread cases achieve different PAPR performances depending on the phase shift pattern. There exist substantial PAPR differences between the ITSM-conditioned cases (pattern number $=1$ in Table I) and the non-ITSM-conditioned cases (pattern number $=2\sim7$ in Table I). In [11] and [12], the authors proposed a DFT-spread FBMC with the pattern number $=2$. The PARR curves in Fig. 3 reveal that the pattern number 2 of all occasions achieves the worst PAPR performance. For instance, at CCDF of 10^{-3}, the DFT spreading with the phase shift pattern 2 achieves a PAPR reduction of around 1.1 dB compared to the pure FBMC. On the other hand, the DFT spreading with the ITSM conditioned phase shift pattern achieves PAPR reduction of around 1.9 dB. Also in [13], the PAPR result of another DFT-spread FBMC is provided where we find almost the same PAPR reduction (approximately 1.1 dB) against the pure FBMC as that of the DFT-spread FBMC in [11]. This implies that the phase shift pattern employed in [13] is not ITSM-conditioned either.

It can be confirmed that by ITSM-conditioned phase shift pattern, the substantial PAPR reduction is further achieved. Moreover, this gain is achieved only by properly setting $\eta_{n,m}$ and $\mu_{n,m}$ without any hardware block or computation complexity overhead. It is also shown that the two ITSM-conditioned phase shift patterns, ((3), (15)) and ((18), (19)) achieve identical PAPR curves. Table I reveals that in many papers on FBMC, the phase shift patterns are non-ITSM-conditioned. As mentioned and confirmed above, the non-ITSM-conditioned pattern does not matter for pure FBMC but matters only for DFT-spread FBMC. However, the problem we note is that even in the DFT-spread FBMCs [11]–[13], the ITSM-conditioned phase shift patterns have never been employed.

The additional PAPR reduction by the ITSM-conditioned phase shift pattern over the non-ITSM-conditioned phase shift patterns is limited to 0.6 dB $\sim$ 0.8 dB. This is because the single carrier effect is achieved only in the overlapped interval between the IQ channels of the OQAM symbol. Moreover, even in the overlapped interval, the single carrier signal is imperfectly made because of non-rectangular pulse shaping. To overcome this limitation, we introduce a further improved scheme employing a candidate selection idea in the next subsection.

IV. Combining a Candidate Selection Scheme With the ITSM-Conditioned and DFT-Spread FBMC

The PAPR reduction of the proposed scheme is accomplished by two factors. Firstly, in order to maximize the single carrier effect of DFT spreading, the waveform is generated basically based on the ITSM-conditioned FBMC, as derived in the previous section. Secondly, in order to boost the PAPR reduction, we generate multiple versions (actually four distinct versions) of the ITSM-conditioned FBMC waveforms which include the versions by ((3), (15)) and ((18), (19)). The four versions are then compared with each other and the one with the smallest peak power is selected and transmitted.

A. Structure and Algorithm of the Proposed DFT-Spread FBMC Transmitter and Receiver

The data frame is divided into consecutive blocks, each of which contains W FBMC symbols. Regarding the second factor of the proposed PAPR reduction scheme mentioned above, we generate four versions of the DFT-spread and ITSM-conditioned FBMC waveforms for each data block. First two versions for the lth data block denoted by $x_l^{(1)}(t)$ and $x_l^{(2)}(t)$ are made equal to (16) and (17), respectively, with the symbol index m limited to the lth data block, i.e., $lW \le m \le (l+1)W-1$ as follows:

$$x_l^{(1)}(t) = \sum_{n=0}^{N-1}\sum_{m=lW}^{(l+1)W-1}(-1)^m\left\{A_{n,m}h(t-mT) + jB_{n,m}h\left(t-mT-\frac{T}{2}\right)\right\}e^{jn\frac{2\pi}{T}(t+\frac{T}{4})}, \quad (22)$$

$$x_l^{(2)}(t) = \sum_{n=0}^{N-1}\sum_{m=lW}^{(l+1)W-1}(-1)^m\left\{A_{n,m}h(t-mT) + jB_{n,m}h\left(t-mT-\frac{T}{2}\right)\right\}e^{jn\frac{2\pi}{T}(t-\frac{T}{4})}. \quad (23)$$

Note that the subcarriers in (23) are just $T/2$ time shifted versions of those in (22). Assuming rectangular pulse shaping for the sake of simplicity, (22) and (23) in the IQ overlapped interval of each FBMC symbol are the single carrier signals with time shift $T/4$ and $-T/4$, respectively. On the other hand, in the outside of the overlapped interval, each FBMC symbol overlaps with the consecutive FBMC symbols, and therefore the different time shift in the multicarrier results in quite different waveforms. Therefore, the peak powers of the two waveforms are also different from each other.

In (22) and (23), the Q channel is one-half symbol-delayed for OQAM modulation prior to multicarrier modulation. Even if the I channel instead of the Q channel is one-half symbol delayed, the FBMC signal format and the ITSM condition are still satisfied. Hence, for the other two versions for the lth data block denoted by $x_l^{(3)}(t)$ and $x_l^{(4)}(t)$, we consider the modified versions of (22) and (23), respectively, where the I channel is delayed instead of the Q channel, as follows:

$$x_l^{(3)}(t) = \sum_{n=0}^{N-1}\sum_{m=lW}^{(l+1)W-1}(-1)^m\left\{A_{n,m}h(t-mT-\frac{T}{2}) + jB_{n,m}h\,(t-mT)\right\}e^{jn\frac{2\pi}{T}(t+\frac{T}{4})}, \quad (24)$$

$$x_l^{(4)}(t) = \sum_{n=0}^{N-1}\sum_{m=lW}^{(l+1)W-1}(-1)^m\left\{A_{n,m}h(t-mT-\frac{T}{2}) + jB_{n,m}h\,(t-mT)\right\}e^{jn\frac{2\pi}{T}(t-\frac{T}{4})}. \quad (25)$$

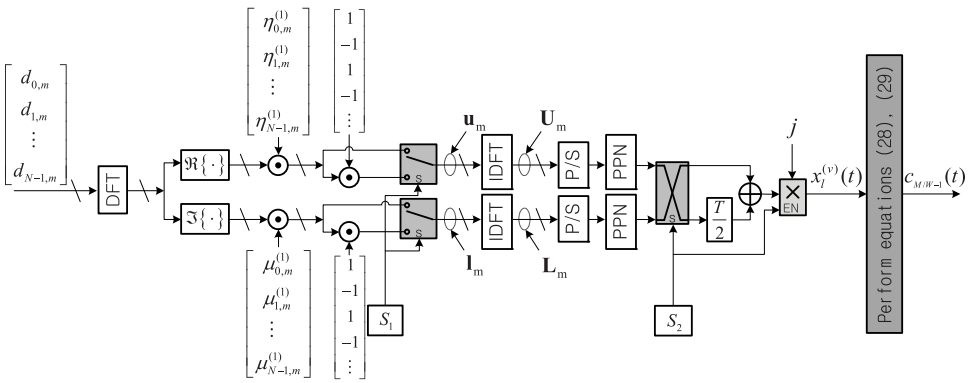

Fig. 4. Transmitter of the proposed FBMC, $\odot$ denotes element-by-element multiplication.

As the symbols in the IQ overlapped periods remain the same irrespective of the delay in I or Q channel, (24) and (25) are equal to (22) and (23), respectively in the IQ overlapped interval, assuming rectangular pulse for simplicity. However, depending on which channel is delayed, the peak powers of the two versions are different. This is explained as follows: The delayed channel symbol overlaps the subsequent OQAM symbol and the non-delayed channel symbol overlaps the preceding symbol. Therefore, the parts of the signal outside the overlapped interval are different depending on which channel is delayed and thus, the overall waveforms of the two versions are different. Summing up, the peak powers of the four waveforms in (22), (23), (24) and (25) are different each other and this inspired us to add a candidate selection idea to the ITSM-conditioned and DFT-spread FBMC.

Similarly as done in Section III-A and Section III-B, we can show that $\eta_{n,m}$ and $\mu_{n,m}$ for $x_l^{(3)}(t)$ in (24) are identical to (18) and (19), respectively and $\eta_{n,m}$ and $\mu_{n,m}$ for $x_l^{(4)}(t)$ in (25) are identical to (3) and (15), respectively. Thus, if we let $\eta_{n,m}^{(v)}$ and $\mu_{n,m}^{(v)}$ denote $\eta_{n,m}$ and $\mu_{n,m}$ for $x_l^{(v)}(t)$, respectively, then $\eta_{n,m}^{(1)} = \eta_{n,m}^{(4)} = (-1)^m j^n$,$\mu_{n,m}^{(1)} = \mu_{n,m}^{(4)} = (-1)^m j\ (-j)^n$ and $\eta_{n,m}^{(2)} = \eta_{n,m}^{(3)} = (-1)^m(-j)^n$, $\mu_{n,m}^{(2)} = \mu_{n,m}^{(3)} = (-1)^m(j)^{n+1}$. In other words, we can generate $x_l^{(3)}(t)$ and $x_l^{(4)}(t)$ by using identical settings for $\eta_{n,m}$ and $\mu_{n,m}$ as those used for $x_l^{(2)}(t)$ and $x_l^{(1)}(t)$, respectively. The only difference is that the I channel is delayed instead of the Q channel. Therefore, in Fig. 2 which is the implementation structure for $x_l^{(2)}(t)$ and $x_l^{(1)}(t)$, we need to delay the upper PPN output instead of the lower PPN output.

Comparing $\eta_{n,m}^{(1)}$ and $\eta_{n,m}^{(2)}$, we have $\eta_{n,m}^{(2)} = \begin{cases} \eta_{n,m}^{(1)} & n = \text{even} \\ -\eta_{n,m}^{(1)} & n = \text{odd}, \end{cases}$ and comparing $\mu_{n,m}^{(1)}$ and $\mu_{n,m}^{(2)}$, we have $\mu_{n,m}^{(2)} = \begin{cases} \mu_{n,m}^{(1)} & n = \text{even} \\ -\mu_{n,m}^{(1)} & n = \text{odd}. \end{cases}$ From this relation, we can generate $x_l^{(2)}\left(\text{or } x_l^{(3)}(t)\right)$ by simply alternating the polarities of the odd number indexed IDFT inputs in the implementation structure for generating $x_l^{(1)}(t)\left(\text{or } x_l^{(4)}(t)\right)$ as shown in Fig. 4. The four versions of the waveform are generated respectively by setting two switching control bits S_1 and S_2 as shown in Table II. For ease of comparison with the previous DFT-spread FBMC, the additional blocks are shaded. They include only polarity inversions and two switching blocks. Hence, hardware-wise, the complexity overhead is negligible.

TABLE II
SWITCHING RULE FOR THE FOUR VERSIONS OF THE WAVEFORM

Version	Switching control bit S_1	Switching control bit S_2
$x_l^{(1)}(t)$	0	0
$x_l^{(2)}(t)$	1	0
$x_l^{(3)}(t)$	1	1
$x_l^{(4)}(t)$	0	1

Note that in (22) and (23), j is multiplied to the delayed channel, whereas in (24) and (25), j is multiplied to the preceding channel. This does not matter if we transmit only the lth data block. However, we need to concatenate (add) the consecutive data blocks, which breaks FBMC signal format. For example, we cannot add $x_l^{(3)}(t)\ \left(\text{or } x_l^{(4)}(t)\right)$ to $x_{l-1}^{(1)}(t)\ \left(\text{or } x_{l-1}^{(2)}(t)\right)$. In order to avoid this problem, we modify (24) and (25) by simply multiplying these equations by j as follows:

$$x_l^{(3)}(t) = \sum_{n=0}^{N-1} \sum_{m=lW}^{(l+1)W-1} (-1)^m \Big\{ jA_{n,m}h(t - mT - \frac{T}{2}) - B_{n,m}h\,(t - mT) \Big\} e^{jn\frac{2\pi}{T}(t+\frac{T}{4})}, \quad (26)$$

$$x_l^{(4)}(t) = \sum_{n=0}^{N-1} \sum_{m=lW}^{(l+1)W-1} (-1)^m \Big\{ jA_{n,m}h(t - mT - \frac{T}{2}) - B_{n,m}h\,(t - mT) \Big\} e^{jn\frac{2\pi}{T}(t-\frac{T}{4})}. \quad (27)$$

In (26) and (27), j is multiplied to the delayed channel as in (22) and (23), and this allows the addition of consecutive data blocks irrespective of their ITSM condition versions. This modification is implemented using a conditional multiplier at the final stage of Fig. 4. This multiplication is enabled exceptionally for the versions 3 and 4 and thus, it is controlled by S_2.

Overall, the transmit waveform is generated as follows: Starting from the first ($l = 0$) block, we select the candidate achieving the minimum peak power and then successively

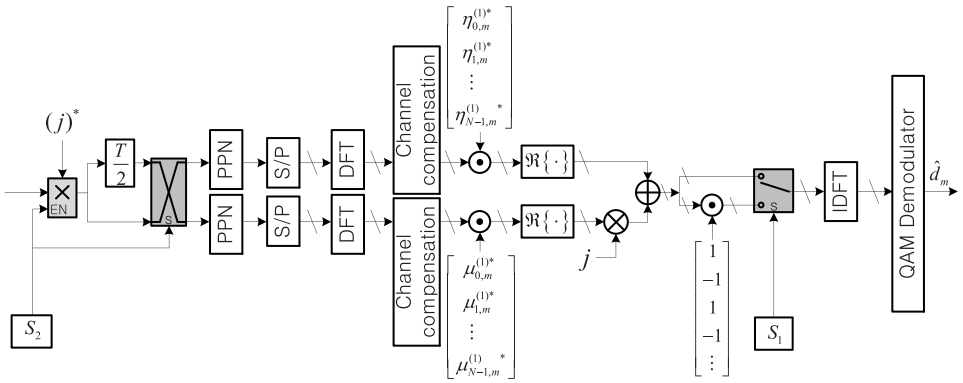

Fig. 5. Receiver of the proposed FBMC, $\odot$ denotes element-by-element multiplication.

concatenate the selected candidates. Let $c_l(t)$ denote the concatenated waveform up to the lth block, then it is generated as follows:

$$c_l(t) = c_{l-1}(t) + x_l^{(k_l)}(t), \quad \text{with } c_{-1}(t) = 0, \tag{28}$$

where k_l is the selected candidate index of the lth block through the following calculation:

$$k_l = \begin{cases} \underset{v\in\{1,2,3,4\}}{\arg\min} \left\{ \max\limits_{t\in R} \left| x_l^{(v)}(t) \right|^2 \right\}, & \text{if } l = 0 \\ \underset{v\in\{1,2,3,4\}}{\arg\min} \left\{ \max\limits_{t\in R} \left| c_{l-1}(t) + x_l^{(v)}(t) \right|^2 \right\}. & \text{else.} \end{cases} \tag{29}$$

The peak power search zone R is limited to the time zone of the current data block waveform $x_l^{(v)}(t)$. Thus, considering the pulse shaping, R is set to $\left[lWT - \frac{KT}{2}, (l+1)WT + \frac{T}{2} + \frac{KT}{2}\right]$. Also from (29), note that for $l \geq 1$, we need to find the peak power of not $x_l^{(v)}(t)$ but $c_{l-1}(t) + x_l^{(v)}(t)$, because $c_{l-1}(t)$ and $x_l^{(v)}(t)$ overlap due to the pulse shaping and IQ staggering of OQAM.

The receiver for the proposed scheme is implemented as shown in Fig. 5. Compared to the receiver of the previous DFT-spread FBMC, there is no difference except that there are two switching blocks that are controlled by the received SI. Thus, the receiver computation complexity is identical to that of the previous DFT-spread FBMC.

B. Complexity Efficient Transmitter of the Proposed FBMC

Apparently, the transmitter side algorithm that was provided in the last part of Section IV-A requires the FBMC modulation to be performed four times in each data block for generating the four candidate versions. However, we can reduce the practical computation complexity by equivalently modifying some of the processes and maximizing the shared portions for generating the four versions. In this subsection, we propose a complexity efficient transmitter of the proposed FBMC, which, compared to the previous DFT-spread FBMC, requires only one more operation for upper and lower PPNs in Fig. 2, respectively.

Let us find the redundant calculation between the cases $S_1 = 0$ and $S_1 = 1$. For the ease of explanation, the upper IDFT input vectors in Fig. 4 are denoted by $\mathbf{u}_m$. As $\mathbf{u}_m$ changes depending on the switching control bit S_1, let us further specify $\mathbf{u}_m^{(S_1=0)}$ as $\mathbf{u}_m$ for $S_1 = 0$ and specify $\mathbf{u}_m^{(S_1=1)}$ as $\mathbf{u}_m$ for $S_1 = 1$.

From Fig. 4, we can see that

$$\begin{aligned} \mathbf{u}_m^{(S_1=1)} &= [1, -1, 1, -1, \cdots, -1] \odot \mathbf{u}_m^{(S_1=0)} \\ &= e^{j\pi\{0:(N-1)\}} \odot \mathbf{u}_m^{(S_1=0)} \end{aligned} \tag{30}$$

where $\odot$ denotes element-by-element multiplication. Let us denote the IDFT output vectors of $\mathbf{u}_m^{(S_1=0)}$ and $\mathbf{u}_m^{(S_1=1)}$ by $\mathbf{U}_m^{(S_1=0)}$ and $\mathbf{U}_m^{(S_1=0)}$, respectively, i.e., $\mathbf{U}_m^{(S_1=0)} = \text{IDFT}\left[\mathbf{u}_m^{(S_1=0)}\right]$, $\mathbf{U}_m^{(S_1=1)} = \text{IDFT}\left[\mathbf{u}_m^{(S_1=1)}\right]$ where IDFT[$\mathbf{x}$] indicates the IDFT output vector with the input vector $\mathbf{x}$. Assume that N is an even integer such as a power of 2 for low complexity IDFT. Then, by the relation in (30) and the cyclic time shift property of the discrete Fourier transform, we get

$$\mathbf{U}_m^{(S_1=1)} = \left[\mathbf{U}_m^{(S_1=0)}(N/2 : N-1)\ \mathbf{U}_m^{(S_1=0)}(0 : N/2-1)\right] \tag{31}$$

which is equivalent to swapping the left and the right half parts of $\mathbf{U}_m^{(S_1=0)}$. Similarly, if we denote the two versions of the lower IDFT input vector according to S_1 in Fig. 4 by $\mathbf{l}_m^{(S_1=0)}$ and $\mathbf{l}_m^{(S_1=1)}$, respectively, then, we get

$$\mathbf{L}_m^{(S_1=1)} = \left[\mathbf{L}_m^{(S_1=0)}(N/2 : N-1)\ \mathbf{L}_m^{(S_1=0)}(0 : N/2-1)\right], \tag{32}$$

i.e., we can also generate the IDFT output vector $\mathbf{L}_m^{(S_1=1)}$ simply by swapping the left and the right half parts of $\mathbf{L}_m^{(S_1=0)}$. Note that even with zero padding to the IDFT inputs, the rules (31) and (32) hold. We only need to replace N in (31) and (32) by the zero padded input size.

Consequently, the complexity efficient transmitter of the proposed scheme is implemented as shown in Fig. 6. As the two switching controls are placed after the IDFT, all the operations from DFT to IDFT need to be performed only once. The switching control by S_1 is placed right after the IDFT. Hence, the PPNs (upper and lower) need to be performed twice, one for the case with $S_1 = 0$ and the other for $S_1 = 1$. As only the delay and addition remain after the switching control S_2, the additional computation for generating the waveform with $S_2 = 1$ is negligible if the one with

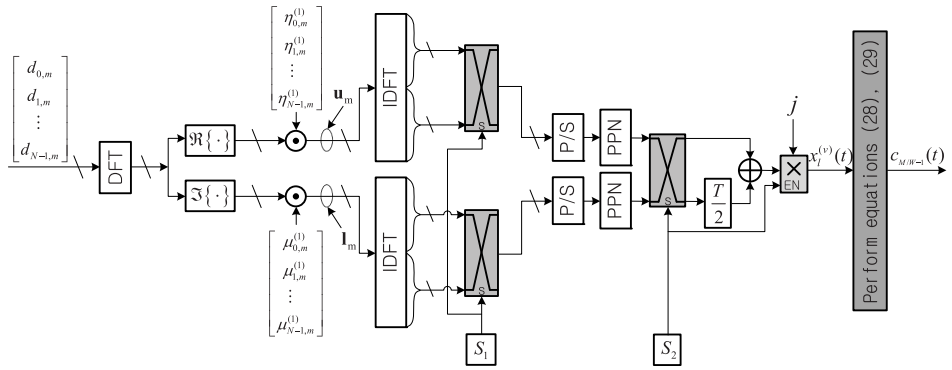

Fig. 6. Complexity efficient transmitter of the proposed FBMC, ⊙ denotes element-by-element multiplication.

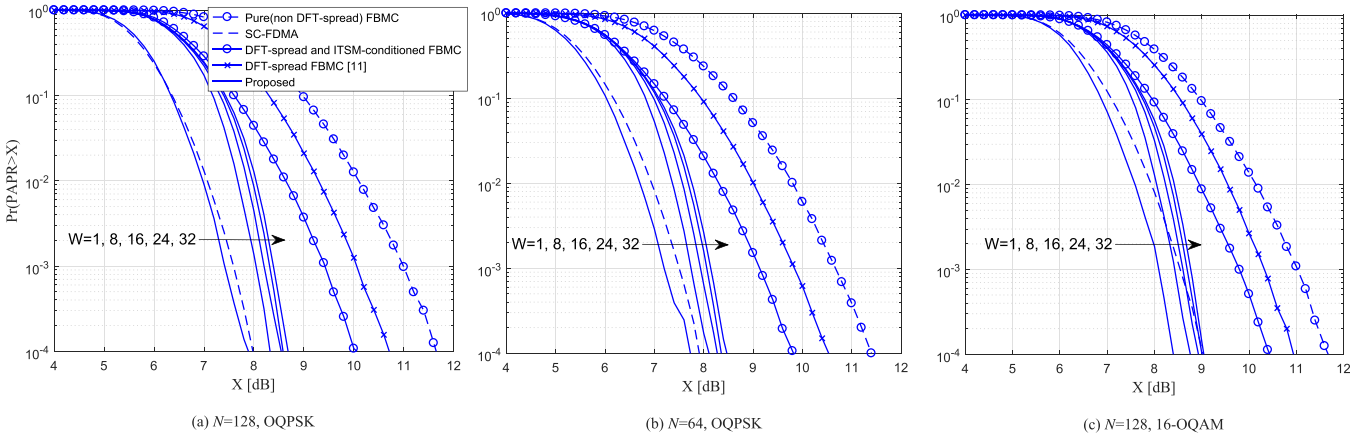

(a) N=128, OQPSK (b) N=64, OQPSK (c) N=128, 16-OQAM

Fig. 7. CCDFs of PAPR for the different FBMC schemes.

$S_2 = 0$ has been generated first. Compared to the previous DFT-spread FBMC, the proposed DFT-spread FBMC performs PPN computations twice for both the upper and lower parts in Fig. 6, one for generating $x_l^{(1)}(t)$ and $x_l^{(4)}(t)$ and the other for generating $x_l^{(2)}(t)$ and $x_l^{(3)}(t)$.

V. Performance Comparisons With the Other PAPR Reduction Schemes for FBMC

We first compare the proposed scheme with the pure (non DFT-spread) FBMC and the previous DFT-spread scheme based on the simulated PAPR results. Then, in Table III, the comparisons are extended to the other PAPR reduction schemes for FBMC.

Fig. 7 shows the PAPR's CCDF curves of the schemes being compared for OQPSK with $N = 128$, OQPSK with $N = 64$ and 16 OQAM with $N = 128$, respectively. The PAPR's CCDF curves of the pure FBMC and the previous DFT-spread scheme are also included for the comparison. The proposed scheme achieves significant PAPR reduction. For instance, at CCDF of 10^{-3} in Fig. 7(a), the proposed scheme with $W = 8$ achieves about 3.0 dB reduction compared to the pure FBMC, 2 dB reduction compared to the conventional DFT-spread FBMC in [11] and 1.4 dB reduction compared to the DFT-spread and ITSM-conditioned FBMC. It is remarkable that the proposed scheme with $W = 1$ achieves even lower PAPR compared to SC-FDMA. This is because in addition to DFT spreading, the proposed scheme has another factor for further PAPR reduction, i.e., selection among the four waveform variations having different peak powers.

As two bit SI is generated per data block, we need to set the block size W to be sufficiently large if the system demands high bandwidth efficiency. It is intuitive that as the block size increases, the PAPR reduction gain of the proposed scheme will decrease. However, it is remarkable that with a larger W, i.e., $W = 32$, the PAPR reduction gains of the proposed scheme against the pure FBMC and the conventional DFT-spread FBMC are still substantial. We can find almost the same trends in Fig. 7(b) and Fig. 7(c). Moreover, in the case of higher modulation order in Fig. 7(c), the proposed scheme even with a large W ($W = 32$) maintains the PAPR just 0.25 dB above that of the SC-FDMA at a CCDF of 10^{-3}. This behavior of the proposed scheme leads to a distinguishable feature, i.e., low PAPR with negligible SI overhead. Meanwhile, the larger W results in the higher demodulation latency. Thus, W should be properly set considering a tradeoff between SI overhead and latency.

In order to properly assess the proposed scheme in terms of its design goal, i.e., low PAPR, low computational complexity and ignorable SI overhead, we compare these three factors among the various PAPR reduction schemes for FBMC in Table III. We included the schemes in [5] and [8] for the

TABLE III
COMPARISONS AMONG THE PAPR SCHEMES FOR FBMC

Scheme	SI bits per frame	PAPR reduction over pure FBMC at CCDF=10^{-3}		Computations per symbol period	
		N=64, OQPSK	N=128, OQPSK	Major calculations	No. of RMs with N=128,K=4,L_o=4
Pure FBMC	0	0 dB	0 dB	2 IDFTs, 2 PPNs	24576
DFT-spread FBMC [11, 13]	0	1 dB	1 dB	1 DFT, 2 IDFTs, 2 PPNs	26368
DFT-spread and ITSM-conditioned FBMC	0	1.9 dB	2 dB	1 DFT, 2 IDFTs, 2 PPNs	26368
Proposed scheme	$2M/W$	2.5 dB with W=32, 3.0 dB with W=8, 3.5 dB with W=1	2.6 dB with W=32, 3.0 dB with W=8, 3.6 dB with W=1	1 DFT, 2 IDFTs, 4 PPNs	38656
PTS for FBMC [5] with V partitions and the segment length of L	MV/L	2.42 dB with V=4, L=6 2.55 dB with V=4, L=4 2.85 dB with V=4, L=2		$2V$ IDFTs, $4VN2^V$ RMs, 2 PPNs	122880 with V=4
ISLM for FBMC [8] with U candidates	$M\log_2 U$	2 dB with U=8		$2UN$ RMs, $2U$ IDFTs, $2U$ PPNs	206848 with U=8

comparison, because they have been referred to as the two typical PAPR reduction scheme for FBMC, and are based on PTS and SLM, respectively. Instead of simulating the schemes in [5] and [8] which are rather cumbersome, we consider the values from the CCDF curves of PAPR provided in those papers for comparison. The column labeled *PAPR reduction* in Table III refers to the PAPR threshold ($=X$) difference (in dB at CCDF $= 10^{-3}$) between each scheme and the same reference, i.e., the pure FBMC, which has been also termed as the *original* FBMC in [5] and [8]. Although [5] and [8] do not provide the PAPR results for $N = 128$, we presume that the PAPR reductions for $N = 128$ will be almost the same as the PAPR reduction for $N = 64$ in Table III. This presumption is well justified by comparing the PAPR reductions for $N = 64$ and 128 for the other schemes in Table III.

Overall, the proposed scheme outperforms the schemes in [5] and [8] in all the three aspects, i.e., PAPR gain, SI overhead and computation complexity. The proposed scheme requires much smaller SI compared to the schemes in [5] and [8]. This is because the candidate version in the proposed scheme is selected at each block, not each FBMC symbol [8] or small segment [5]. For instance, for a frame length of $M = 96$, the proposed scheme with block size $W = 32$ transmits only 6 bit SI per frame, whereas the scheme in [5] with the number of partitions $V = 4$ and the segment length $L = 6$ transmits 64 bit SI per frame and the scheme in [8] with the number of candidates $U = 8$ transmits 288 bit SI per frame. Moreover, even with much smaller SI, the proposed scheme achieves better PAPR performance than those of the schemes in [5] and [8]. It is remarkable and rather against our intuition that only the block-wise peak minimization with only the four candidates in the proposed scheme achieves lower PAPR compared to the symbol-wise or small segment-wise peak minimizations with the numerous candidate combinations throughout each frame in the PTS or SLM schemes. This is because unlike other schemes, the candidates of the proposed scheme are already DFT-spread with the ITSM condition for single carrier effect, and thus even with only four candidates, the overall PAPR reduction is very substantial.

Regarding the computation complexity in Table III, for fair comparison, we assume that the basic FBMC modulation parts of all the schemes being compared are identically implemented as shown in Fig. 1(a), which is one of the complexity efficient implementations among the state of art FBMC modulators [14], [15]. Recall that in Fig. 1(a), the individual pulse shaping in each subcarrier and multicarrier modulation are equivalently implemented only by two IDFTs and two PPNs. Hence, we accordingly converted the complexity formulae in [5] to highly reduced versions and inserted them in Table III.

For the sake of simplicity, the number of additions are not considered, because multiplication requires much higher computation complexity than addition. Assuming that N is a power of 2, the number of RMs (real multiplications) of N-point DFT is given as $4\times\ (N/2)\log_2 N$ [29], where the factor 4 denotes the number of RMs per one complex multiplication. For a fair comparison of complexity, we assume that the $4N$ point IDFTs with $3N$ zero padding are used in all the schemes being compared. The numbers of RMs for the $4N$-point IDFT with $3N$ zeros padded to the input is given as $4\times\ (2N\log_2 N + 2N)$, not $4\times 2N\log_2(4N)$ [29]. Fig. 1(b) shows that the PPN needs $8KN(=2\times K\times 4N)$ RMs per symbol duration, because the PPN input (= IDFT output) with a sample size of $4N$ is complex-valued whereas the pulse sample is real-valued.

Summing up the number of RMs required for each item in the column *Major calculations* in Table III, the total complexities for PTS in [5], SLM in [8], and the proposed scheme are expressed as $16VN\log_2\ N + (2^{V+2}+16)VN + 16KN + 2^{V+3}N$, $16UN\log_2 N + 16UKN + 26UN$ and $18N\log_2 N + 32KN + 48N$, respectively. From these general expressions, we can show that as N increases, the complexity ratio of the proposed sheme to the PTS asymptotically goes to $\frac{9}{8V}$ and the complexity ratio of the proposed scheme to the SLM asymptotically goes to $\frac{9}{8U}$. In accordance with our intuition, the complexity ratio is inversely proportional to V and U and thus, with the nominal values of V and U, the computation complexity of the proposed scheme is much lower compared to PTS and SM. For instance, with $N = 128$ and $K = 4$, the proposed scheme needs only about 31.5 % and 18.7 % RMs compared to the PTS with $V = 4$ as set in [5] and the SLM with $U = 8$ as set in [8], respectively.

To view the actual FBMC spectrum in a practical system, we need to add the effect of HPA (high power amplifier) nonlinearity to the spectrum. As a simple and efficient assessment of the HPA nonlinearity effect, we consider a SEL (soft envelop limiter) model [2]. The HPA nonlinearity of the SEL

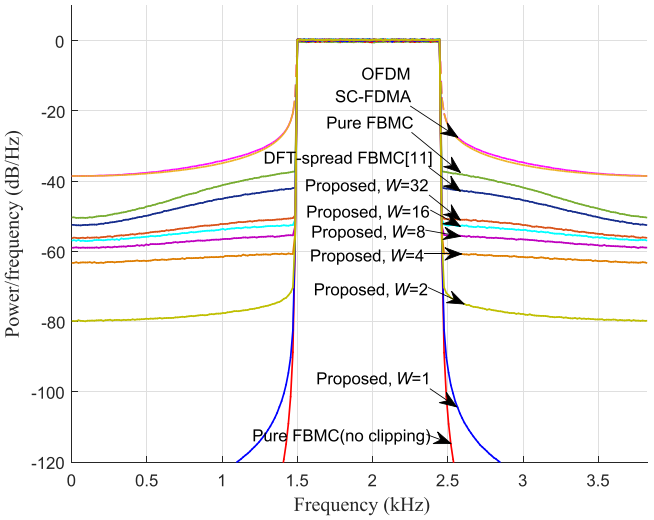

(a) A^2=7dB above the mean power

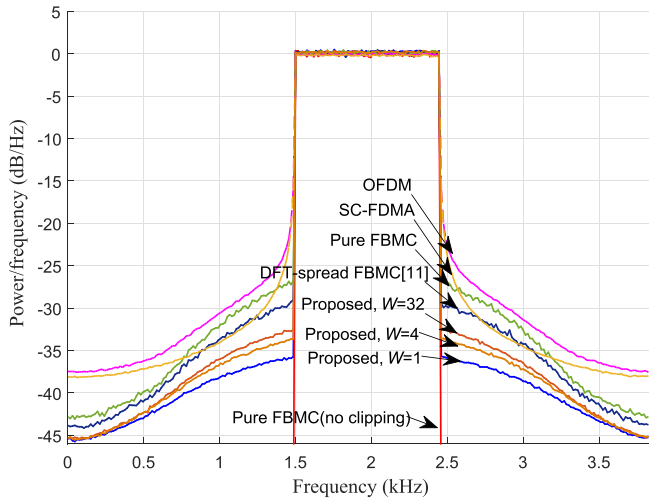

(b) A^2=5dB above the mean power

Fig. 8. Spectra of various FBMC signals with the amplitudes clipped, $N = 64$, 16-OQAM.

model is given as $\tilde{x}(t) = \begin{cases} x(t), & \text{if } |x(t)| \le A, \\ Ae^{j\angle x(t)}, & \text{if } |x(t)| > A \end{cases}$ where A is the clipping level and $\tilde{x}(t)$ is the output of the HPA, whose input is the original complex signal $x(t)$. Fig. 8 shows the spectra of various FBMC schemes when the waveforms pass through HPA nonlinearity with clipping power levels of $A^2 = 7$ dB and 5 dB above the mean power. Note that the y-axes of the two subplots have the different scales for better presentation. For reference, the spectrum of the FBMC signal without clipping is also included, which validates the outstanding feature of FBMC over OFDM and SC-FDMA, i.e., the excellent suppression of OOB power emission.

However, it is also shown that this outstanding feature of FBMC deteriorates if the FBMC signal undergoes HPA nonlinearity. For instance, for $A^2 = 7$ dB above the mean power, both the pure FBMC and the previous DFT-spread FBMC have significant regrowth in the OOB spectrum and the gaps to those of OFDM or SC-FDMA decrease. For tighter clipping, i.e., $A^2 = 5$ dB above the mean power, the OOB spectra of both systems partially become even higher than that of SC-FDMA.

On the other hand, owing to the reduced PAPR, the proposed scheme significantly suppresses the OOB spectrum regrowth. For $A^2 = 7$ dB above the mean power, the proposed scheme with $W = 1$ maintains the OOB suppression very close to that of the unclipped FBMC. Even with $W = 32$ for negligible SI overhead, the proposed scheme still maintains a fairly low OOB spectrum compared to the existing schemes. For tighter clipping, i.e., with $A^2 = 5$ dB above the mean power, there is reduction in the OOB spectrum gaps among the schemes. However, it should be noted that the proposed scheme with $W = 1$ has quite lower OOB spectrum among the schemes. Although the merit of negligible SI overhead diminishes for $W = 1$, two bit SI per FBMC symbol (=SI overhead for $W = 1$) is still lower than the nominal values for the other SI-based schemes. Overall, even with HPA nonlinearity, the proposed FBMC scheme performs excellent OOB spectrum suppression over OFDM or SC-FDMA.

VI. Conclusions

In this paper, we proposed a low PAPR FBMC scheme and confirmed its outstanding performance compared to the existing PAPR reduction schemes in terms of PAPR reduction gain, computation complexity overhead and SI overhead. We first derived the so called ITSM (identically-time-shifted-multicarrier) condition, which fully exploits the single carrier effect of DFT spread FBMC. Then, in order to further enhance the amount of PAPR reduction, we generate the four candidate versions of the DFT-spread and ITSM-conditioned FBMC waveform and select the one with minimum peak power. Using the proposed scheme, we resolved a pending issue of FBMC, i.e., OOB spectrum regrowth due to HPA nonlinearity. We showed that even with the HPA nonlinearity, the proposed scheme substantially suppresses the OOB spectrum regrowth and still achieves the best spectrum localization among the schemes in comparison.

References

[1] T. Ihalainen, T. H. Stitz, M. Rinne, and M. Renfors, "Channel equalization in filter bank based multicarrier modulation for wireless communications," *EURASIP J. Adv. Signal Process.*, vol. 2007, Dec. 2007, Art. no. 49389.

[2] J. Vihriala, N. Ermolova, E. Lahetkangas, O. Tirkkonen, and K. Pajukoski, "On the waveforms for 5G mobile broadband communications," in *Proc. IEEE VTC Spring*, May 2015, pp. 1–5.

[3] S. S. K. C. Bulusu, H. Shaiek, and D. Roviras, "Prediction of spectral regrowth for FBMC-OQAM system using cumulants," in *Proc. IEEE WiMob*, Oct. 2014, pp. 402–406.

[4] D. Qu, S. Lu, and T. Jiang, "Multi-block joint optimization for the peak-to-average power ratio reduction of FBMC-OQAM signals," *IEEE Trans. Signal Process.*, vol. 61, no. 7, pp. 1605–1613, Apr. 2013.

[5] C. Ye, Z. Li, T. Jiang, C. Ni, and Q. Qi, "PAPR reduction of OQAM-OFDM signals using segmental PTS scheme with low complexity," *IEEE Trans. Broadcast.*, vol. 60, no. 1, pp. 141–147, Mar. 2013.

[6] G. Cheng, H. Li, B. Dong, and S. Li, "An improved selective mapping method for PAPR reduction in OFDM/OQAM system," *Commun. Netw.*, vol. 5, no. 3, pp. 53–56, Sep. 2013.

[7] S. S. K. C. Bulusu, H. Shaiek, D. Roviras, and R. Zayani, "Reduction of PAPR for FBMC-OQAM systems using dispersive SLM technique," in *Proc. ISWCS*, Aug. 2014, pp. 26–29.

[8] A. Skrzypczak, J.-P. Javaudin, and P. Siohan, "Reduction of the peak-to-average power ratio for OFDM/OQAM modulation," in *Proc. IEEE VTC-Spring*, May 2006, pp. 2018–2022.
[9] Y. Zhou, T. Jiang, C. Huang, and S. Cui, "Peak-to-average power ratio reduction for OFDM/OQAM signals via alternative-signal method," *IEEE Trans. Veh. Technol.*, vol. 63, no. 1, pp. 494–499, Jan. 2014.
[10] S. Lu, D. Qu, and Y. He, "Sliding window tone reservation technique for the peak-to-average power ratio reduction of FBMC-OQAM signals," *IEEE Wireless Commun. Lett.*, vol. 1, no. 4, pp. 268–271, Aug. 2012.
[11] T. Ihalainen, A. Viholainen, T. H. Stitz, M. Renfors, and M. Bellanger, "Filter bank based multi-mode multiple access scheme for wireless uplink," in *Proc. EUSIPCO*, vol. 9. Aug. 2009, pp. 1354–1358.
[12] A. Viholainen, M. Bellanger, and M. Huchard. (2009). *PHYDAS-PHYsical Layer for Dynamic AccesS and Cognitive Radio Report D5.1*. [Online]. Available: www.ict-phydyas.org/delivrables/PHYDYAS-D5-1.pdf
[13] C. H. Yuen, P, Amini, and B. Farhang-Boroujeny, "Single carrier frequency division multiple access (SC-FDMA) for filter bank multicarrier communication systems," in *Proc. CROWNCOM*, Jun. 2010, pp. 1–5.
[14] M. Bellanger, D. L. Ruyet, D. Roviras, and M. Terre, *FBMC Physical Layer: A Primer* PHYDYAS FP7 Project Document, Jan. 2010.
[15] M. Terre. FBMC Modulation/Demodulation, MATLAB Central. Accessed: Jan. 21, 2014. [Online]. Available: https://www.mathworks.com/matlabcentral/fileexchange
[16] D. Na and K. Choi, "Intrinsic ICI-free alamouti coded FBMC," *IEEE Commun. Lett.*, vol. 20, no. 10, pp. 1971–1974, Oct. 2016.
[17] L. Varga and Z. Kollár, "Low complexity FBMC transceiver for FPGA implementation," in *Proc. IEEE RADIOELEKTRONIKA*, Jun. 2013, pp. 219–223.
[18] B. Farhang-Boroujeny, "OFDM versus filter bank multicarrier," *IEEE Signal Process. Mag.*, vol. 28, no. 3, pp. 92–112, May 2011.
[19] J. Du and S. Signell, "Time frequency localization of pulse shaping filters in OFD/OQAM systems," in *Proc. IEEE ICASP*, Dec. 2007, pp. 1–5.
[20] T. Ihalainen, A. Ikhlef, J. Louveaux, and M. Renfors, "Channel equalization for multi-antenna FBMC/OQAM receivers," *IEEE Trans. Veh. Technol.*, vol. 60, no. 5, pp. 2070–2085, Jun. 2011.
[21] R. Zakaria and D. Le Ruyet, "A novel filter-bank multicarrier scheme to mitigate the intrinsic interference: Application to MIMO systems," *IEEE Trans. Wireless Commun.*, vol. 11, no. 3, pp. 1112–1123, Mar. 2012.
[22] Y. Medjahdi, M. Terre, D. Le Ruyet, D. Roviras, and A. Dziri, "Performance analysis in the downlink of asynchronous OFDM/FBMC based multi-cellular networks," *IEEE Trans. Wireless Commun.*, vol. 10, no. 8, pp. 2630–2639, Aug. 2011.
[23] M. Payaró, A. Pascual-Iserte, and M. Nájar, "Performance comparison between FBMC and OFDM in MIMO systems under channel uncertainty," in *Proc. IEEE EW*, Apr. 2010, pp. 1023–1030.
[24] M. Hazewinkel, "Dirichlet kernel," in *Encyclopedia of Mathematics*. Rotterdam: The Netherlands: Springer, 2001.
[25] P. Siohan, C. Siclet, and N. Lacaille, "Analysis and design of OFDM/OQAM systems based on filterbank theory," *IEEE Trans. Signal Process.*, vol. 50, no. 5, pp. 1170–1183, May 2002.
[26] Z. Kollar, L. Varga, and K. Czimer, "Clipping-based iterative PAPR-reduction techniques for FBMC," in *Proc. InOWo*, Aug. 2012, pp. 1–12.
[27] M. Caus and A. I. Perez-Neira, "Transmitter-receiver designs for highly frequency selective channels in MIMO FBMC systems," *IEEE Trans. Signal Process.*, vol. 60, no. 12, pp. 6519–6532, Dec. 2012.
[28] Z. Kollár, L. Varga, B. Horváth, P. Bakki, and J. Bitó, "Evaluation of clipping based iterative PAPR reduction techniques for FBMC systems," *Sci. World J.*, vol. 2014, Jan. 2014, Art. no. 841680.
[29] C.-L. Wang and Y. Ouyang, "Low-complexity selected mapping schemes for peak-to-average power ratio reduction in OFDM systems," *IEEE Trans. Signal Process.*, vol. 53, no. 12, pp. 4652–4660, Dec. 2005.

Dongjun Na received the B.S. and M.S. degrees from Yeungnam University, Gyeongsan, South Korea, in 2014 and 2016, respectively, where he is currently pursuing the Ph.D. degree with the Department of Information and Communication Engineering. His current interests include physical layer for 5G and beyond communication systems.

Kwonhue Choi received the B.S., M.S., and Ph.D. degrees in electronic and electrical engineering from the Pohang University of Science and Technology, Pohang, South Korea, in 1994, 1996, and 2000, respectively. From 2000 to 2003, he was with the Electronics and Telecommunications Research Institute, Daejeon, South Korea, as a Senior Research Staff. In 2003, he joined the Department of Information and Communication Engineering, Yeungnam University, Gyeongsan, South Korea, where he is currently a Professor. He is co-author of the text book entitled *Problem-Based Learning in Communication Systems Using MATLAB and Simulink* (Wiley, 2016). His research area includes signal design for the communication systems, multiple access schemes, diversity schemes for wireless fading channels, and multiple antenna systems.